

## Full length article

## Evolution of dislocation structure in neutron irradiated Zircaloy-2 studied by synchrotron x-ray diffraction peak profile analysis



T. Seymour<sup>a</sup>, P. Frankel<sup>a</sup>, L. Balogh<sup>b</sup>, T. Ungár<sup>a, c</sup>, S.P. Thompson<sup>d</sup>, D. Jädernäs<sup>e</sup>, J. Romero<sup>f</sup>, L. Hallstadius<sup>g</sup>, M.R. Daymond<sup>b</sup>, G. Ribárik<sup>c, h</sup>, M. Preuss<sup>a, \*</sup>

<sup>a</sup> Materials Performance Centre, School of Materials, The University of Manchester, Manchester, M13 9PL, UK

<sup>b</sup> Department of Materials and Engineering, Nicol Hall, Queen's University, Kingston, ON, K7L 3N6, Canada

<sup>c</sup> Department of Materials Physics, Eötvös University Budapest, PO Box 32, H-1518, Budapest, Hungary

<sup>d</sup> Diamond Light Source, Harwell Science and Innovation Campus, Didcot, Oxfordshire, OX11 0DE, UK

<sup>e</sup> Studsvik Nuclear AB, SE 611 82, Nyköping, Sweden

<sup>f</sup> Westinghouse Electric Company, Columbia, SC, USA

<sup>g</sup> Westinghouse Electric Sweden AB, SE 72163, Västerås, Sweden

<sup>h</sup> Laboratory of Excellence on Design of Alloy Metals for low-mAss Structures (DAMAS), Université de Lorraine, France

## ARTICLE INFO

## Article history:

Received 1 May 2016

Received in revised form

10 November 2016

Accepted 13 December 2016

Available online 28 December 2016

## Keywords:

Synchrotron diffraction

Peak profile analysis

Irradiation effects

Dislocation density

Zirconium alloys

## ABSTRACT

Dislocation structures in neutron irradiated Zircaloy-2 fuel cladding and channel material have been characterized by means of high-resolution synchrotron x-ray diffraction combined with whole peak profile analysis and by transmission electron microscopy (TEM). The samples available for this characterization were taken from high burnup fuel assemblies and offer insight into the evolution of the dislocation structure after the formation of dislocation loops containing a *c* component. Absolute dislocation density values are about 4–15 times higher for the whole peak profile compared to TEM analysis. Most interestingly, the diffraction analysis suggests that the total dislocation density, as well as the *a* loop density, increases with fluence for the cladding material type. This trend is also inferred from a Williamson-Hall representation but contradicts the TEM observations. The *c* loop density evolution is more complicated and doesn't display any particular trend. In addition, the diffraction analysis highlights the presence of well-developed shoulders adjacent to the basal reflections and noticeable peak asymmetry particularly for the channel samples that experienced slightly lower operation temperatures than the clad. The findings are discussed in respect of the perceived irradiation induced growth mechanisms in Zr alloys.

© 2017 Acta Materialia Inc. Published by Elsevier Ltd. This is an open access article under the CC BY license (<http://creativecommons.org/licenses/by/4.0/>).

## 1. Introduction

Zirconium alloys are widely used by the nuclear industry as fuel cladding and reactor core structural material due to their low neutron absorption cross-section, suitable mechanical properties and good corrosion resistance. Despite these advantageous characteristics, zirconium cladding exhibits dimensional instabilities in the high temperature irradiation environment of a nuclear reactor, which are a result of irradiation induced growth, irradiation enhanced creep and hydrogen pick up [1–3]. Irradiation growth is, in the case of zirconium fuel cladding with a typical split basal

texture, the volume conserving axial expansion and radial contraction of the clad under fast neutron irradiation ( $E > 1$  MeV) that is independent of applied stress. Irradiation growth has been observed to be dependent on neutron fluence [4], temperature [5,6], alloy composition [7] and thermomechanical history (crystallographic texture and degree of dislocation density in the processed material) [8,9] but a detailed mechanistic understanding is presently absent.

In recrystallised zirconium alloys with a typical split basal texture, the initial stage of growth is correlated with the formation of dislocation loops characterized by a Burgers vector of  $\frac{1}{2}1\bar{1}20$  and a loop plane normal distributed between the first and second order prismatic planes [10–12]. They are either of vacancy or interstitial character, and are commonly referred to as *a* loops. During service strongly textured and recrystallised Zr alloys show some initial

\* Corresponding author.

E-mail addresses: [thomas.seymour@postgrad.manchester.ac.uk](mailto:thomas.seymour@postgrad.manchester.ac.uk) (T. Seymour), [michael.preuss@manchester.ac.uk](mailto:michael.preuss@manchester.ac.uk) (M. Preuss).

rapid growth followed by a slow steady state growth phase. The initial growth phase is associated with an increase in total dislocation line density of  $a$  loops [13,14], while transmission electron microscopy (TEM) investigations have reported  $a$  loop number density saturation during the steady state growth phase [15]. After the period of limited growth a threshold fluence is reached where a second stage of accelerated or “breakaway growth” occurs [6,16]. Breakaway growth in neutron-irradiated Zr alloys has been correlated with the irradiation-induced formation of large faulted vacancy dislocation loops with a Burgers vector of  $\frac{1}{2}\langle 110 \rangle$  that lie on the basal plane [4,17] and are hereafter referred to simply as  $c$  loops. The nucleation mechanism for  $c$  loops is not fully understood, but is believed to be related to the presence of diffusing solute elements from dissolving precipitates [18].

The characterisation and quantification of dislocation loops in irradiated nuclear reactor materials has traditionally been limited to TEM analysis, as it enables direct imaging of the line defects. However, it is very time consuming to perform statistically reliable measurements of dislocation densities in a TEM, particularly for irradiated materials where it can be challenging to distinguish the dislocation loops from other sources of contrast [11,17]. Therefore, quantitative assessments of dislocation densities from TEM measurements are lacking, especially at high fluences where the  $a$  loop density is large and the newly formed  $c$  loops tend to be of greater interest. For mechanically deformed materials the development and implementation of diffraction peak profile analysis (DPPA) has facilitated the study of bulk dislocation structure in [19–21]. DPPA allows for indirect, but statistically reliable, measurements of dislocation density and population distribution [22], providing a complementary technique to TEM analysis [23].

In the present study the aim was to investigate the dislocation structure of a set of Zircaloy-2 samples extracted from fuel cladding and channel boxes, irradiated in boiling water reactors to fluences between  $8.7 \times 10^{25} \text{ n m}^{-2}$  and  $14.7 \times 10^{25} \text{ n m}^{-2}$  ( $E > 1 \text{ MeV}$ ) [24,25], via DPPA, to elucidate the high fluence dislocation evolution and compare the data with conventional dislocation analysis by bright field TEM imaging. In order to achieve this, diffraction profiles were recorded on the I11 beamline at the Diamond Light Source [26], UK, which have been analysed using the extended Convolutional Multiple Whole Profile (CMWP) analysis procedure [19,27–29].

## 2. Experimental methods

### 2.1. Material

Westinghouse Electric Company and Studsvik Nuclear AB supplied neutron-irradiated, recrystallised Zircaloy-2 samples [24] in the form of six electro-polished TEM foils. The nominal chemical composition of the material, together with the details of the foils, is presented in Table 1, in order of increasing neutron fluence. Of the six foils, four were extracted from fuel cladding of the

Westinghouse designated LK3™ type [30] from the Leibstadt (KKL) boiling water reactor (BWR), one foil was taken from a channel box sample from KKL and one foil was extracted from a channel box sample from the Olkiluoto-2 (OL-2) BWR. The channel boxes are manufactured by following a processing path similar to the cladding, i.e. melting, hot-rolling and  $\beta$ -quenching, followed by a series of cold-rolling/annealing steps culminating in a final recrystallisation anneal.

It is difficult to acquire a good selection of material that has been neutron irradiated in controlled, identical conditions to different fluences. The investigation of cladding and channel together is not ideal, as the two structures are in different neutron environments and experience a temperature difference [31] of approximately  $50^\circ\text{C}$ , however the material presently studied is what was most readily available.

In addition, Westinghouse Electric Company also supplied recrystallised non-irradiated LK3™ type Zircaloy-2 sheet, which was used to prepare a non-irradiated reference bulk sample by standard mechanical grinding and polishing.

The total in-reactor elongation strain data associated with the cladding material is shown in Fig. 1. It is evident from the linear elongation strain of the cladding and the high neutron fluences, all of which are above the  $3\text{--}4 \times 10^{25} \text{ n m}^{-2}$  generally accepted threshold fluence range for initiation of breakaway growth [32], that these samples have experienced breakaway growth. However, it should be noted that the samples came from a functioning fuel assembly and as such was not stress-free during service, therefore the strain represents both irradiation-induced growth and irradiation-enhanced creep as well as strains derived from oxide and hydride formation and pellet-cladding interaction [3,33].

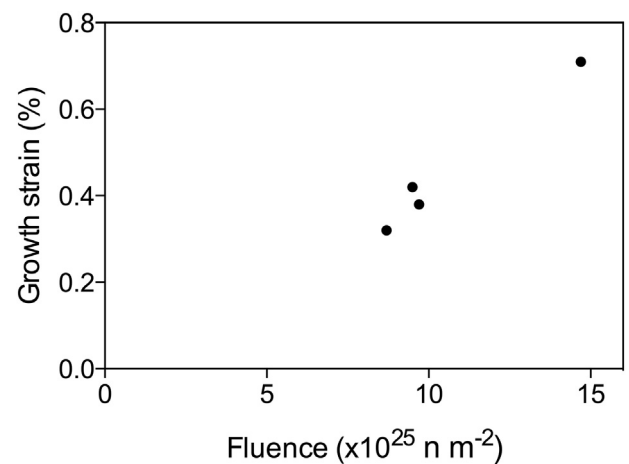


Fig. 1. Growth strain of 4-meter Zircaloy-2 fuel rods derived from rod growth data in Table 1.

Table 1

Neutron irradiated Zircaloy-2 sample data with \* indicating cladding samples, \*\* indicating channel samples from Leibstadt BWR and \*\*\* indicating channel samples from Olkiluoto-2 BWR.

Chemical composition (wt.%): 1.34–1.35 Sn, 0.17–0.18 Fe, 0.11 Cr, 0.05–0.07 Ni						
Sample	# cycles	Rod average neutron fluence ( $10^{25} \text{ n m}^{-2}$ )	Rod growth (mm)	Approx. core elevation (mm)	Rod average burnup (MWd/kg)	
1*	5	8.7	12.7	2700	51.1	
2*	6	9.5	16.6	2700	57.3	
3*	7	9.7	15.3	1100	57.4	
4***	5	11	N/A	N/A	N/A	
5**	7	13.1	N/A	N/A	N/A	
6*	9	14.7	28.4	2100	78.7	

## 2.2. Synchrotron XRD

Synchrotron X-ray diffraction measurements were carried out at the high resolution powder diffraction beamline I11 at the Diamond Light Source, UK [26,34]. The high angular resolution (detection width  $\Delta 2\theta \sim 0.003^\circ - 0.009^\circ$  at 15 keV and  $2\theta = 10^\circ - 50^\circ$ ) and low background (electronic noise  $< 0.15$  counts  $s^{-1}$ ), attained by using multi-analysing crystal (MAC) detectors, allows for accurate determination of the peak shape needed for DPPA. The near-parallel beam, small energy bandwidth and use of analyser crystals gives a narrow instrumental profile that can be accounted for to obtain high quality quantitative information.

Two separate synchrotron experiments were necessary in order to limit the total activity of the samples present at the beamline. This resulted in two slightly different X-ray wavelengths of 0.82616 Å during the first campaign (samples 1, 3, 4 and 5) and 0.8256 Å during the second campaign (samples 2 and 6), both calibrated against NIST SRM 640c standard Si reference powder. In the first campaign, the sample holder required the spot size of the beam to be slit down to  $200 \mu\text{m} \times 200 \mu\text{m}$ , which was sufficient to produce high intensity, high quality peaks over 20 min scans. Scans were taken from two foil orientations to account for sample texture and four positions within the foil per orientation to account for sample inhomogeneity. The resulting profiles were averaged, with the individual profiles also being analysed to give an indication of variability. In the second campaign an improved sample holder arrangement and alignment meant that a beam size of  $500 \mu\text{m} \times 500 \mu\text{m}$  could be used. One scan per foil was taken from the orientation producing patterns with strong basal peaks. The reduction in number of scans per foil was necessary due to experimental time constraints, but the larger spot size meant similar volumes were sampled for each experiment.

The irradiated samples were studied in transmission geometry, Fig. 2a, through the thin central region of the electro-polished TEM foils in order to maximize the diffraction signal. Multiple samples

were held in a holder allowing for only one period of set up time whilst taking data from multiple samples using a remote controlled stage to move each of the four samples into the beam consecutively. As the sample holder imposed some angular restrictions, the set up allowed the recording of approximately 20 diffraction peaks depending on the crystallographic texture of the sampled volume.

Reflection geometry was used for the bulk, non-irradiated sample as shown in Fig. 2b. In this case, a beam geometry was used that resulted in a footprint of  $1 \times 1 \text{ mm}^2$  with the angle between the beam direction and normal to the sample surface set at  $5^\circ$ . The scan time was 30 min and the sampling statistics were further improved by spinning the sample at 1200 rpm about the sample surface normal.

## 2.3. Transmission electron microscopy

The TEM dislocation analysis was performed by Studsvik Nuclear AB using a JEOL 2100F operated at 200 kV in bright field mode [35–37]. In order to image different types of dislocations, two beam conditions were set up in the microscope using different g-vectors depending on dislocation Burgers vector. The g-vectors  $g = (0004)$  and  $g = (10\bar{1}0)$  were used for counting c-type and a-type dislocation loops, respectively. Foil thickness measurements were taken using a standard electron energy loss spectroscopy (EELS) technique. Electron Energy Loss Spectroscopy (EELS) was employed to measure the foil thickness in each image field. For each image field, a wide energy range loss spectrum was acquired and the zero-loss peak (ZLP) extracted using standard routines. The integrals under the ZLP,  $I_0$ , and under the whole spectrum,  $I$  was then calculated. The thickness,  $t$ , is then calculated as  $t = (\ell) * \ln(I/I_0)$ . A tabulated value for the mean free path for inelastic electron scattering,  $\ell$ , was used [38]. At least 5 images from different grains were taken at  $40,000\text{--}60,000\times$  magnification for a loop analysis and at  $80,000\text{--}120,000\times$  magnification for c loop analysis. The foil thickness measurements were assumed to have a 3% error and the relative uncertainty in counting a and c loops were set to  $2\sqrt{n}/n$  and  $\sqrt{n}/n$ , respectively, where the increased difficulty in detecting a loop leads to the greater uncertainty.

## 3. Diffraction peak profile analysis

Diffraction peak profile analysis has been used to quantify the dislocation structures introduced by irradiation. Under the correct conditions, X-ray radiation will undergo Bragg scattering from a crystalline material. For a perfect crystal, and fully coherent monochromatic radiation, all diffracted intensity occurs at a single angle for each lattice plane resulting in a set of sharp Bragg peaks. However, if there is distortion of the crystal due to micro-strain [39],  $I_{\text{strain}}$ , small size crystallites [40],  $I_{\text{size}}$ , or faulting [28,29],  $I_{\text{fault}}$ , the diffracted intensity is distributed over a range of angles resulting in Bragg peak broadening. In practice, instrumental broadening,  $I_{\text{instrument}}$ , resulting from the energy spread of the beam, beam divergence, scattering from the air, detection geometry, etc, also contributes to the shape of the Bragg peaks. Hence, the resulting measured profile,  $I_{\text{measured}}$ , is a convolution of the individual broadening components:

$$I_{\text{measured}} = I_{\text{size}} * I_{\text{strain}} * I_{\text{fault}} * I_{\text{instrument}} \quad (1)$$

According to the Krivoglaz-Wilkens model [41–44], the theoretical strain broadening profile for a single peak ( $I_{\text{hkl}}^D$ ) is given by its Fourier coefficient,  $A_{\text{hkl}}^D$ :

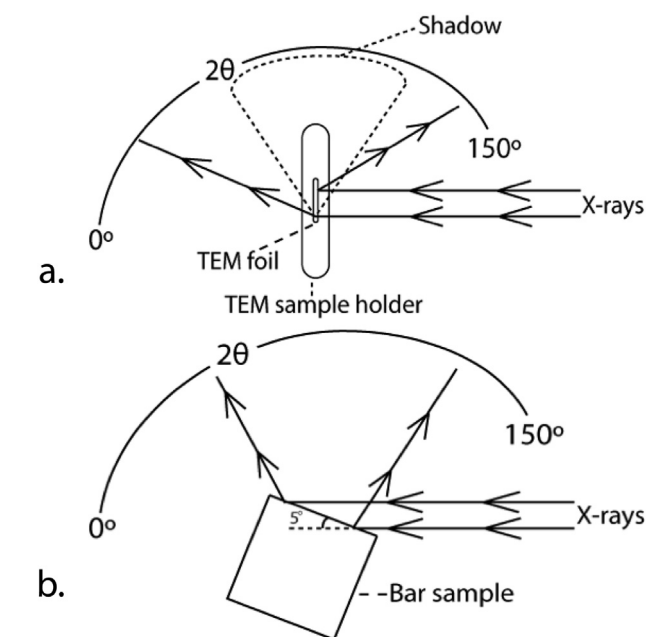


**Fig. 2.** Schematic of the sample setup at beamline I11 at the Diamond Light Source synchrotron showing a) transmission sample geometry, used for irradiated TEM foil sample and b) reflection sample geometry, used for non-irradiated bulk sample spun at 1200 rpm with the sample surface normal maintained at a tilt of  $5^\circ$  with respect to the incident beam.

$$A_L^D = \exp \left[ -\rho \left( \frac{\pi b^2}{2} \right) L^2 f(\eta) g^2 \bar{C} \right] \quad (2)$$

where  $\rho$  is the dislocation density,  $b$  is the magnitude of the Burgers vector,  $L$  is the Fourier variable,  $g$  is the absolute value of the diffraction vector,  $\bar{C}$  is the average contrast factor for dislocations,  $f(\eta)$  is the Wilkens function with  $\eta = L/R_e$ , where  $R_e$  is the effective outer cutoff radius of dislocations in Wilkens' restricted random dislocation distribution [43,44]. The Wilkens arrangement parameter is a dimensionless parameter defined by  $M = R_e \sqrt{\rho}$  [43,44] that quantifies the dislocation dipole character.

The contrast factor for each peak, as included in Eq. (2), is dependent upon the relative orientations of the line and Burgers vectors of the dislocations, the diffraction vector and the elastic constant of the crystal [39,45,46]. In the case of hcp polycrystals the average contrast factor  $\bar{C}_{hkil}$  for the plane  $\{hkil\}$  for a particular dislocation can be written as

$$\bar{C}_{hkil} = \bar{C}_{hki0} (1 + q_1 x + q_2 x^2) \quad (3)$$

$$x = \frac{2}{3} \left( \frac{l}{ga} \right)^2 \quad (4)$$

where  $\bar{C}_{hki0}$  is the average contrast factor for  $\{hki0\}$  planes,  $q_1$  and  $q_2$  are parameters dependent on the elastic constants and dislocation structure [47,48],  $x$  is defined by Eq. (4),  $g$  is defined as before,  $a$  is the basal plane lattice parameter and  $l$  is the fourth order index of the  $\{hkil\}$  plane [49,50].

A hexagonal crystal structure has 11 sub-slip systems [49], characterised by the Burgers vector, slip plane and edge or screw character with each sub-slip system having individual values for  $\bar{C}_{hki0}$ ,  $q_1$  and  $q_2$ . Dragomir and Ungár [49] have numerically calculated these values for zirconium and other hexagonal crystal systems using the freely available ANIZC software [51]. In plastically deformed hcp material the dislocation contrast factors for each sub-slip system can be averaged if all sub-slip systems are randomly populated or if the specimen is a random polycrystal. In such cases, it is possible to determine the relative fractions of dislocations with Burgers vectors of  $a$ ,  $c + a$  and  $c$  type via knowledge of the theoretical and measured average contrast factors [20,52]. Alternatively, different texture components can be considered separately and the contrast factors calculated and procedure altered appropriately. Given the single strong texture component, irradiation homogeneous nature of the loop nucleation and that the irradiation is approximately isotropic, then no analogous considerations need to be made in this study.

For the present work new  $q_1$  and  $q_2$  values had to be numerically calculated to correspond to the irradiation induced dislocation loops, as only contrast factors for straight dislocations were available. However, contrast factors for loops can be calculated by treating the loop as a polygon with  $N$  sides, where  $N$  is a large number [53]. As the contrast factor does not depend on the line length the value corresponding to an infinite straight dislocation line will be the same as the contrast factor of a finite segment with the same Burgers vector, line direction and slip plane vectors. Therefore, the value does not depend on the circumference of the loops either.

The  $a$  loops have been shown to have habit plane normals distributed between  $11\bar{2}0$  and  $10\bar{1}0$  directions [10–12]. As the exact direction of each plane normal between these two vectors is unknown, published loop normal distribution maps [10–12] were used to calculate the weighted average distribution between the  $(11\bar{2}0)$  and the  $(10\bar{1}0)$  habit planes by subdivision of the distribution maps into ten segments, then counting the number of loops in

**Table 2**

Calculated contrast factors,  $\bar{C}_{hkil}$ , and  $q$  parameters,  $q_1$  and  $q_2$ , for circular  $a$  loops with habit planes of  $\{11\bar{2}0\}$  and  $\{10\bar{1}0\}$ , a mixed  $a$  loop population of 30%:70% respectively, and for  $c$  loops.

Dislocation loop	$\bar{C}_{hki0}$	$q_1$	$q_2$
$11\bar{2}0\{10\bar{1}0\}$	0.2539	−0.5454	0.0132
$11\bar{2}0\{11\bar{2}0\}$	0.2579	−0.5046	−0.0031
$20\bar{2}3\{0001\}$	0.0815	2.6411	−0.5563
Mixed $a$ loop population	0.2551	−0.5332	0.0083

each segment to use as weights. This resulted in an average distribution of 30% of  $a$  loops with  $(11\bar{2}0)$  and 70% of  $a$  loops with  $(10\bar{1}0)$  habit planes as used in Table 2.

The  $a$  loops were modeled as perfectly circular loops having a Burgers vector direction of  $[11\bar{2}0]$ , lying on either the  $(10\bar{1}0)$  plane or the  $(11\bar{2}0)$  plane. The  $c$  loop with a Burgers vector direction of  $[20\bar{2}3]$  was modelled as a perfectly circular loop sitting on the  $(0001)$  plane. The multiplicities of the Burgers vectors and loop habit planes were taken into account for every reflection by averaging over all sub-reflections i.e. over  $\{hkil\}$ . In the absence of quantitative TEM measurements of the ellipticity of the  $a$  loops it was assumed that they were circular. This is a reasonable assumption, as interstitial loops are generally circular and vacancy loops in pure Zr have been shown to tend towards circularity with decreasing diameter [11]. The contrast factors for a range of elliptical loops with the major axis aligned along  $[0001]$  were calculated in Ref. [53] and the effects of ellipticity on calculated dislocation density are discussed later.

The average contrast factors as a function of  $x$  for  $a$  and  $c$  loops,  $\bar{C}_{hkil}^a$  and  $\bar{C}_{hkil}^c$  respectively, were calculated using ANIZC [51] for a range of  $x$  as displayed in Fig. 3. In principle, ANIZC can only calculate contrast factors for straight dislocations. Therefore, a program was written in C that can calculate the contrast factors for a dislocation loop with  $n$  straight sides, with each straight side's individual contrast factor being calculated using ANIZC. The contrast factors converged to within a relative error of  $10^{-6}$  when  $n = 274$ , which was taken to be the contrast factor for a circular loop [53]. A quadratic fit to these data resulted in the parameters shown in Table 2. As it can be seen from Fig. 3 and Table 2, the difference in

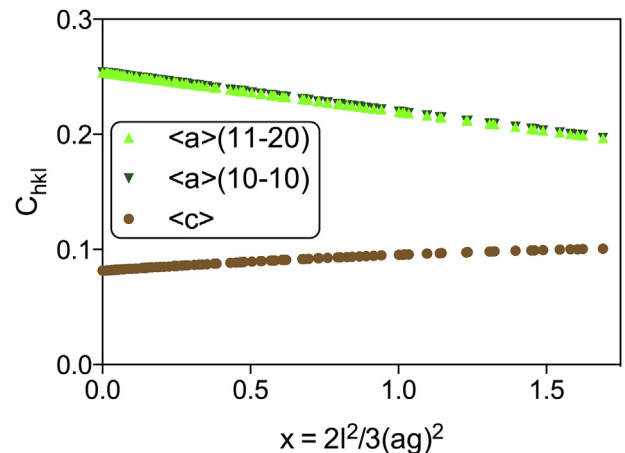


**Fig. 3.** Average contrast factor parabolas described by Eq. (3) for circular dislocation loops modeled with  $11\bar{2}0$  Burgers vector lying on the  $\{10\bar{1}0\}$  planes (dark green) and  $\{11\bar{2}0\}$  planes (bright green), and for  $20\bar{2}3$  Burgers vector loops lying on the  $\{0001\}$  planes (brown), where  $l$  is the fourth index of the reflections,  $a$  is the lattice parameter of the basal plane and  $g$  is the magnitude of the diffraction vector. (For interpretation of the references to colour in this figure legend, the reader is referred to the web version of this article.)



theoretical contrast factors between the two types of  $a$  loop is negligible.

The present calculation procedure of the contrast factors of dislocation loops is, to some extent, an approximation. The straight segments in the polygon representing the loop join at corners. The strain field of dislocations with sharp corners was previously calculated by Yoffe [54]. This work showed that, apart from some simple geometrical factors, the elastic stored energy of dislocations with sharp corners is basically similar to that of infinite straight dislocations. Taking into account that the absolute values of the dislocation densities in our neutron-irradiated specimens can only be given with relatively large error margins, we consider the approximation in Ref. [53] rather satisfactory for the present evaluations. Moreover, the excellent agreement between the dislocation loop types observed by TEM and provided by the CMWP procedure, using the calculated  $q_1$  and  $q_2$  parameter values, is a further indirect evidence that the approximations made in Ref. [53] are reasonable.

For the calculation of the relative fractions of  $a$ ,  $c + a$  and  $c$  dislocations generated by plastic deformation, the sub-slip systems are commonly assumed to be randomly populated [20,52]. However, this method is not appropriate for studying only the two dislocation systems observed in irradiated zirconium. Under these conditions the contribution of each sub system is  $f_i = 1/N_A$ , where  $N_A$  is number of a sub-system, and can only take the values 0, 0.5 or 1 assuming a random population. In order to determine the ratio between the two types of dislocation loops, the method previously formulated in Ref. [20] was modified such that the contribution of each loop system varied systematically from  $f_a = 0$  to  $f_a = 1.0$  (concurrently  $f_c = 1 - f_a = 1.0$  to  $f_c = 0$ ) in steps of 0.01 in order to calculate  $q_{1,2}^{eff}$  as shown in Eq. (5).

$$q_{1,2}^{eff} = \frac{f_a b_a^2 \bar{C}_{hk,0}^a q_{1,2}^a + f_c b_c^2 \bar{C}_{hk,0}^c q_{1,2}^c}{f_a b_a^2 \bar{C}_{hk,0}^a + f_c b_c^2 \bar{C}_{hk,0}^c} \quad (5)$$

Hence,  $q_{1,2}^{eff}$  as a function of  $f_i$  can then be compared systematically to  $q_{1,2}^m$  as described previously [20]. The same tolerance conditions were used to produce histograms where the maximum number of valid solutions for a given  $f_i$  was 1. This produced flat top histograms of height 1, where the middle  $f_a$  and  $f_c$  values in this flat top region were taken as the correct values. Evidently, the width of this region, and hence any indication of error, is set by the tolerance arbitrarily assigned by the user. Therefore any error estimation for the dislocation loop fractions should derive from the size of the tolerance used.

The parameters described above were used in conjunction with the forward modeling peak profile analysis software package, extended Convolutional Multiple Whole Profile (CMWP) [19,27–29] in order to analyse the dislocation density and arrangement. Due to the challenges of evaluating irradiated zirconium diffraction patterns, the efficiency of CMWP has been improved by the incorporation of a Monte Carlo fitting procedure, placing constraints on the range of the fitting parameters, and fitting of the logarithmic intensities to more accurately ascertain the positions and intensities of the shoulders.

#### 4. Results

Fig. 4 is a bright field TEM micrograph displaying the  $a$  and  $c$  loop dislocation structures at  $14.7 \times 10^{25} \text{ n m}^{-2}$ . Several  $a$  and  $c$  loops have been highlighted by red arrows and blue triangles, respectively.

Fig. 5 shows synchrotron X-ray diffraction profiles for non-irradiated Zircaloy-2 and irradiated to  $8.7 \times 10^{25} \text{ n m}^{-2}$ .

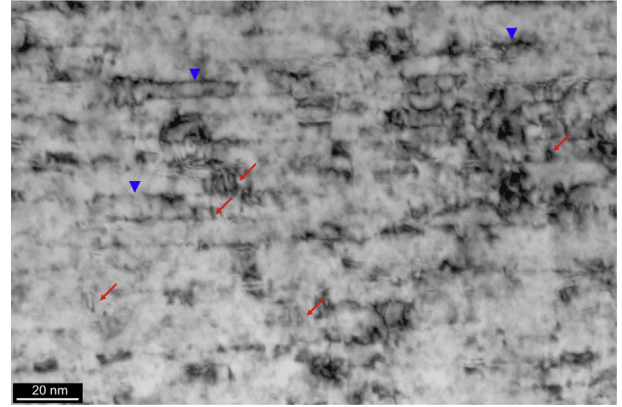


Fig. 4. Bright-field TEM micrograph showing the dislocation structure of neutron-irradiated Zircaloy-2 at a fluence of  $14.7 \times 10^{25} \text{ n m}^{-2}$ . Examples of  $a$  loops have been highlighted by red arrows and  $c$  loops by blue triangles. (For interpretation of the references to colour in this figure legend, the reader is referred to the web version of this article.)

Broadening is clearly observed across a range of Zr peaks. Precipitate peaks are observed in the non-irradiated sample profile, however, these peaks have disappeared after irradiation, indicating either dissolution or amorphisation of the second phase particulates. Most of the peaks have been identified with either  $\text{Zr}_2(\text{Fe,Ni})$  or  $\text{Zr}(\text{Cr,Fe})_2$  precipitates known to be present in Zircaloy-2 [55] although some peaks have not been identified.

Fig. 6 shows examples of basal and prismatic diffraction peaks of Zircaloy-2 before irradiation and after fluences of  $8.7 \times 10^{25} \text{ n m}^{-2}$ ,  $13.1 \times 10^{25} \text{ n m}^{-2}$  and  $14.7 \times 10^{25} \text{ n m}^{-2}$ . It is important to note that the sample exposed to  $13.1 \times 10^{25} \text{ n m}^{-2}$  was channel material while the other two irradiated samples came from clad, irradiated at a temperature  $\sim 50^\circ \text{C}$  hotter than the channel. It is immediately apparent that irradiation causes severe broadening in both basal

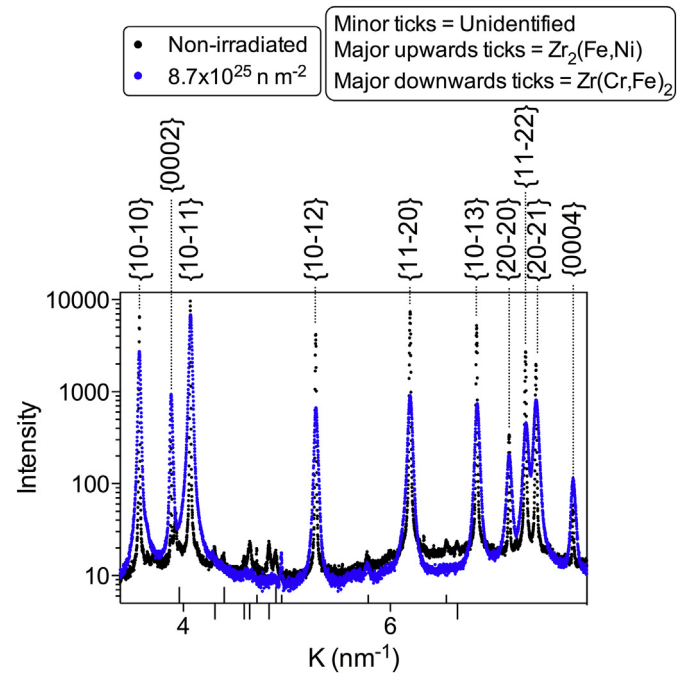
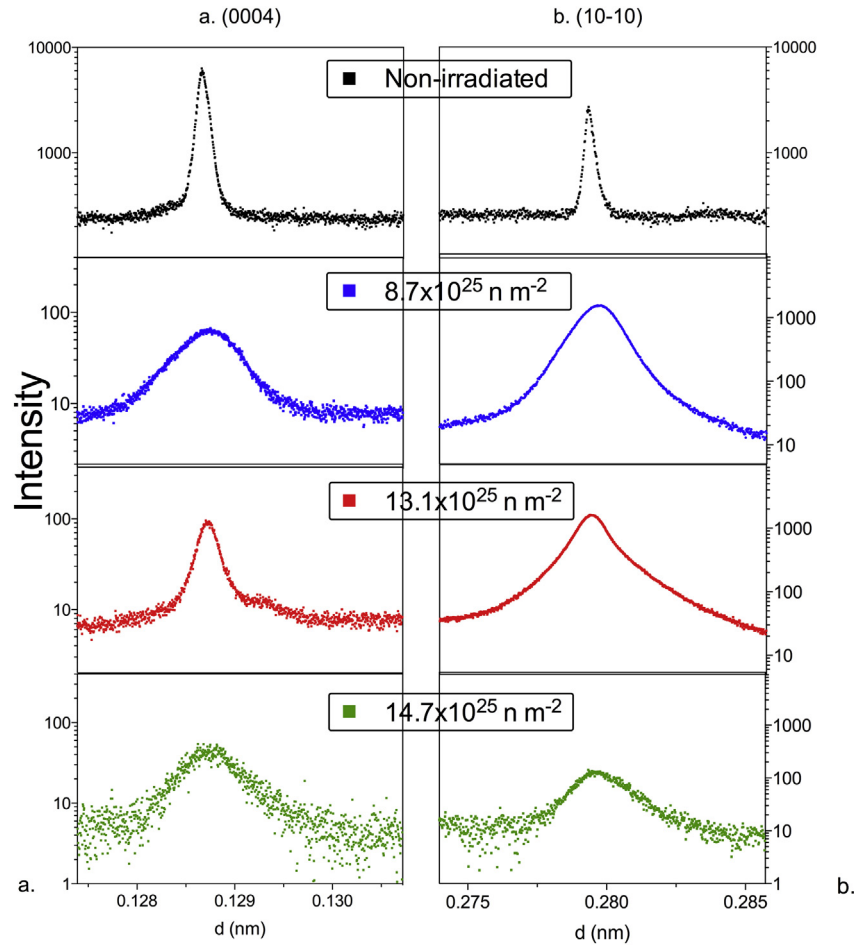


Fig. 5. Synchrotron diffraction profiles for Zircaloy-2 in the non-irradiated condition and irradiated to  $8.7 \times 10^{25} \text{ n m}^{-2}$ . The Zr diffraction peaks are labeled above the profiles, whereas precipitate and peaks of unknown origin are marked below.



**Fig. 6.** Synchrotron diffraction profiles of neutron-irradiated Zircaloy-2 at various fluences for a. the (0004) peak and b. the (10 $\bar{1}0$ ) peak. At  $13.1 \times 10^{25} \text{ n m}^{-2}$  the (0004) peak is narrower than for the cladding at  $8.7 \times 10^{25} \text{ n m}^{-2}$  or at  $14.7 \times 10^{25} \text{ n m}^{-2}$ . The most visible shoulder is on the left hand side of the peak at  $13.1 \times 10^{25} \text{ n m}^{-2}$ . The (10 $\bar{1}0$ ) peak also becomes asymmetric after irradiation. Note the different scales for each peak presented.

and prismatic reflections compared to the non-irradiated state, indicating the presence of *a* and *c* loops. At a fluence of  $8.7 \times 10^{25} \text{ n m}^{-2}$  the peaks for both reflections are fairly symmetrical, however the channel sample irradiated to  $13.1 \times 10^{25} \text{ n m}^{-2}$  displays a noticeably narrower (0004) Bragg peak compared to the lower fluence sample together with a distinct shoulder on the higher *d*-spacing side relative to the Bragg peak. Note that the y-axis in Fig. 6 is in log scale and that the shoulder features are very subtle and may not have been picked up were it not for the low instrumental broadening and high signal-noise ratio on I11, and the use of a log scale. The prismatic peak also presents asymmetry, with the right tail of the Bragg peak becoming extended relative to the left tail. However, as this peak is significantly more broadened than the basal reflection, any underlying shoulder causing this asymmetry is not evident. The basal peak of the clad sample at a fluence of  $14.7 \times 10^{25} \text{ n m}^{-2}$  shows again very significant broadening and significant peak asymmetry, which suggests again the presence of a shoulder towards the higher *d*-spacing side, but now subsumed into the Bragg peak due to its width. The prismatic peak is of very low intensity in this sample due to texture and therefore any features in the peak profile are harder to discern. However, an asymmetry can be recognized as an extension of the right tail relative to the left tail.

A modified Williamson-Hall plot [39,56] of the full width at half-maximum (FWHM) values for two diffraction profiles from the

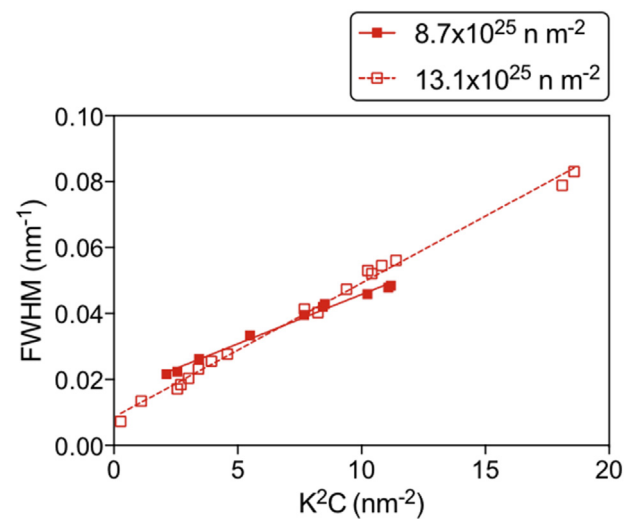


**Fig. 7.** Modified Williamson-Hall plots for the  $8.7 \times 10^{25} \text{ n m}^{-2}$  cladding sample and  $13.1 \times 10^{25} \text{ n m}^{-2}$  channel sample, where the FWHM values originate from the CMWP fit to the peaks. The cladding and channel samples are represented by closed and open symbols respectively. It is clear that the slope of the line is greater for the channel sample than the cladding, meaning that there is more stored energy in the channel sample, i.e. a greater dislocation density.

$8.7 \times 10^{25} \text{ n m}^{-2}$  (cladding) and  $13.1 \times 10^{25} \text{ n m}^{-2}$  (channel) samples is presented in Fig. 7. Only data from two samples are displayed for reasons of clarity. The data points henceforth have been separated into those pertaining to clad (closed symbols) and channel material (open symbols) in order to assist in interpreting the data correctly. The FWHM values have been obtained from the CMWP fit to the peak, i.e. are background subtracted and instrumental broadening free. The slope of the regression line is clearly greater for the channel sample than for the cladding sample, indicating more stored energy, i.e. dislocation density, in the channel sample compared to the cladding sample.

The peak asymmetry and observed shoulders in the irradiated material presented a challenge for the DPPA using CMWP. Initially, fitting trials were carried out using either a fixed Wilkens' arrangement parameter ( $M$ ) or as output from the fitting analysis. In case of a fixed  $M$  a range of values were tried including  $M = 3$  that has been suggested for irradiated Zr pressure tube [21]. The effect of the  $M$  value on the theoretical fit to the measured profile can be seen in Fig. 8a where the right hand side tail of the fit is extended when  $M$  was allowed to vary freely ( $M = 1.6$  for this peak) in comparison to an  $M$  fixed to 3. While the freely varying  $M$  fit is closer to the measured profile on the right hand side of the peak, it overestimates the width of the tail on the left hand side. In contrast, the fixed  $M$  value of 3 captures well the shape of the tail on the left hand side, but delivers a poor fit of the right hand tail. Therefore, standard CMWP analysis gives an erroneous  $M$  value to

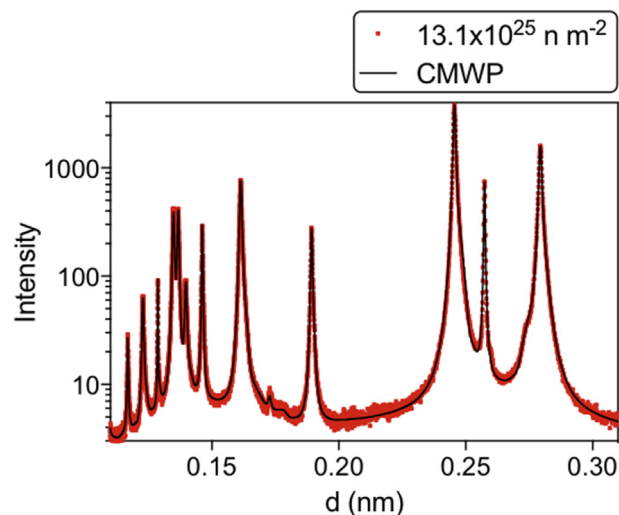


Fig. 9. Example of the CMWP multiphase theoretical fit to a section of the diffraction profile of Zircaloy-2 neutron irradiated to  $13.1 \times 10^{25} \text{ n m}^{-2}$ .

compensate for its inability to accommodate asymmetry and the presence of a shoulder.

In order to overcome this issue the multiphase peak fit option of the CMWP was activated treating the asymmetries and shoulders as a second peak, whose origin is at present unknown. The resulting improvement of the peak fit is illustrated in Fig. 8b. The sum of two peaks gives a more reasonable fit as compared to using a single peak as shown in Fig. 8a. By comparing the single peak fit using  $M = 1.6$  to the main Bragg peak fit of the two phase approach it is observed that the asymmetry does indeed extend the tails of the fit by about 7%. A wider scale example is given in Fig. 9, where it can be seen that the multiphase theoretical pattern matches the measured pattern well across the range of peaks analysed.

The two-peak fitting approach enabled the assessment of the relative fraction of these 'second-phase' peaks relative to the main diffraction peaks using the individual integrated intensities. The fractions of the 'secondary peak' have been plotted in Fig. 10. Generally it is observed that the integrated intensity of these secondary peaks is low compared to the main peak but increases with fluence.

The Wilkens arrangement parameter  $M$  of the main peak obtained for each DPPA analysis is plotted as a function of fluence in

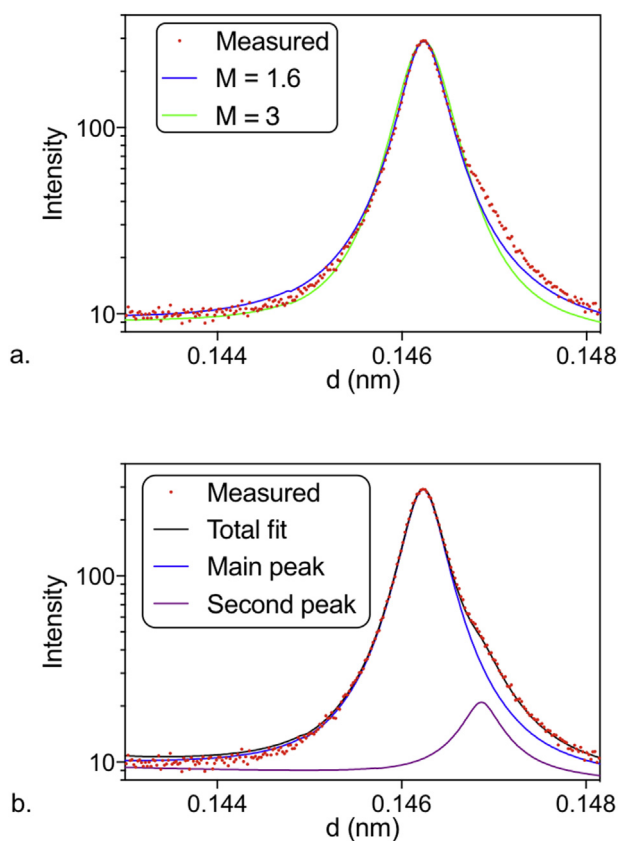


Fig. 8. Example of the CMWP theoretical fits to the  $(10\bar{1}3)$  reflection of Zircaloy-2 neutron irradiated to  $13.1 \times 10^{25} \text{ n m}^{-2}$  a. with  $M$  as a variable determined to be 1.6 (blue) and with  $M$  fixed to 3 (green) and b. using the multiple phase ability of CMWP, where the convolution (black) of a peak fitted to the main Bragg peak (blue) and the secondary peak (purple) gives a good fit to the asymmetric peak. (For interpretation of the references to colour in this figure legend, the reader is referred to the web version of this article.)

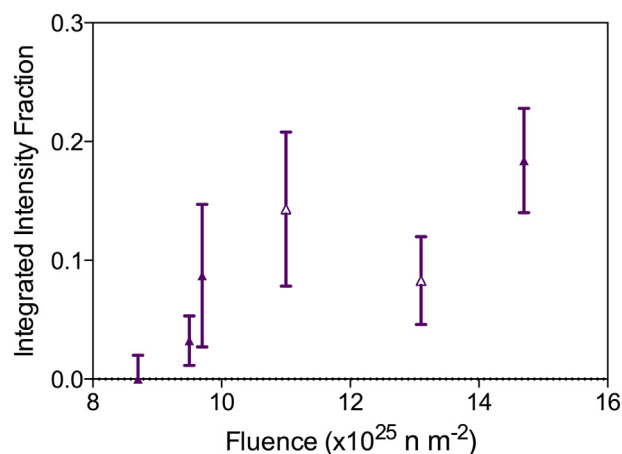
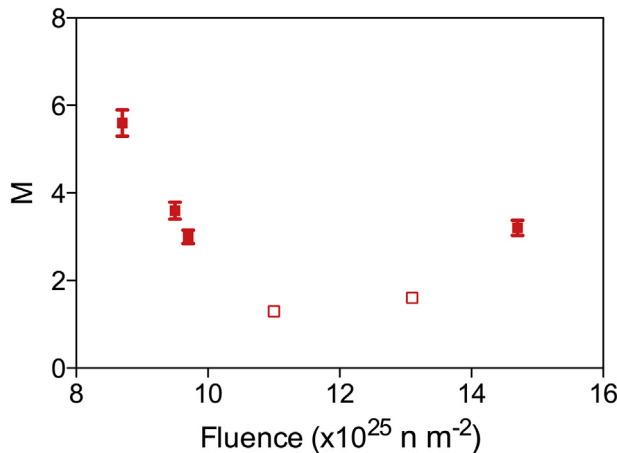


Fig. 10. Fraction of the integrated intensity of the secondary peak relative to the total Bragg diffraction pattern.

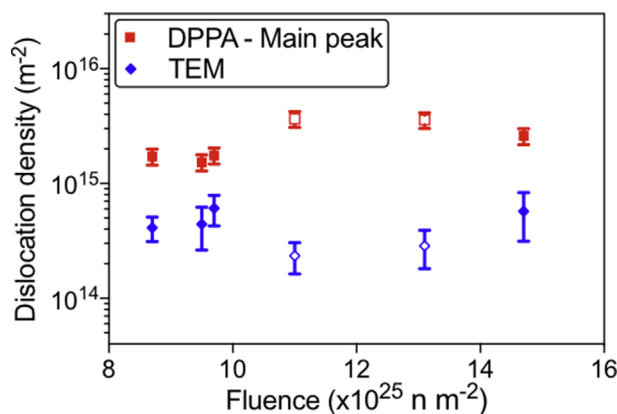


**Fig. 11.** The Wilkens arrangement parameter of the main peak,  $M$ , as a function of fluence. The cladding and channel samples are represented by filled and hollow symbols, respectively.

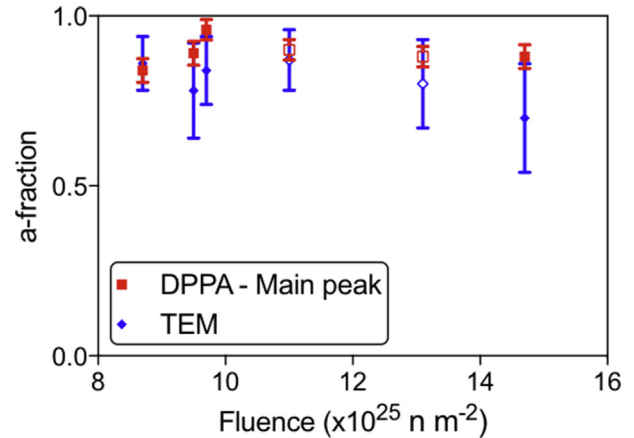
Fig. 11. It can be seen that for the clad samples  $M$  initially drops from about 5.5 to around 3 when reaching  $9.7 \times 10^{25} \text{ n m}^{-2}$  and then remains constant for the highest fluence level. The channel samples show somewhat lower  $M$  values of about 1.5–2.

Fig. 12 shows the dislocation densities calculated from the main Bragg peak using the multiphase peak fit and from TEM measurements [35–37]. The uncertainties displayed here are ~15%, calculated from the uncertainty of the fit and from the uncertainty in calculating the loop fractions from the  $q$ -parameters. The error calculations have not taken into account the potential error from the presence of the second peak, nor from any deviations from the theoretical model used to calculate the dislocation density from the fit, or from the calculation of theoretical contrast factors for loops. It should be noted that the data points from the channel material are again distinguished by using open symbols.

Only considering the clad material, the trends for the dislocation density from DPPA and from TEM measurements are similar for the low fluence samples, however there is a small yet significant increase in dislocation density from  $9.7 \times 10^{25}$  to  $14.7 \times 10^{25} \text{ n m}^{-2}$  as measured by DPPA while the TEM measurements suggest a saturation of defects across these fluences. The channel material shows generally higher dislocation densities than the clad material from DPPA whereas the opposite is true for the TEM measurements.



**Fig. 12.** Dislocation densities determined by CMWP for the main peak (red) and from TEM measurements (blue). The cladding and channel samples are represented by filled and hollow symbols, respectively. Typical statistical errors from the DPPA are ~5%. (For interpretation of the references to colour in this figure legend, the reader is referred to the web version of this article.)



**Fig. 13.** Fraction of  $\langle a \rangle$  loops with fluence determined by CMWP for the main peak (red) and from TEM measurements (blue). The cladding and channel samples are represented by filled and hollow symbols, respectively. (For interpretation of the references to colour in this figure legend, the reader is referred to the web version of this article.)

Comparing the absolute dislocation densities by the two analysis techniques reveals DPPA giving dislocation densities 4–5x higher than the TEM analysis in case of the cladding samples while for the channel material DPPA gives about an order of magnitude higher density values than the TEM analysis.

Fig. 13 illustrates the evolution of  $a$  loop fraction, i.e. the fraction of the total dislocation line density that has a pure  $a$  character, as measured by DPPA considering only the main peak of the two-peak fit and by TEM analysis. Note that the fraction of the total dislocation line density that has a  $c$  character, corresponding to  $c$  loops, is  $1 - a$  fraction. The  $a$  fractions as measured by DPPA are typically close to 0.9 indicating that 90% of the total dislocation line length is comprised of  $a$  loops and does not show evidence of a trend. The  $a$  fraction determined by TEM carries a very high uncertainty as evident from the error bars, which is due to the large uncertainty in the proportion of  $c$  loops contained within a sample foil, when imaged edge on, but seems to sit at the lower value of around 80%. However, despite the suggestion of a decrease in the  $a$  fraction at high fluence, there is no visible trend.

For the DPPA results, the near constant  $a$  line fraction implies that both  $a$  and  $c$  dislocation loop dislocation densities will mirror the trends shown for total density in Fig. 12 and this is indeed what is generally observed in Fig. 14, though Fig. 14b shows a decrease in the  $c$  density for the  $9.7 \times 10^{25} \text{ n m}^{-2}$  sample due to the high  $a$  fraction. The  $a$  loop dislocation density in Fig. 14a shows that the discrepancies in results between TEM and DPPA are 4–5x for cladding and over an order of magnitude for the channel, similar to the total dislocation density shown in Fig. 12. The difference in  $c$  loop dislocation densities between the two analysis techniques tends to be slightly smaller for the cladding material while the channel samples again show a discrepancy between DPPA and TEM that is in the order of magnitude range, Fig. 14b.

## 5. Discussion

Traditionally, quantitative assessments of the irradiation-induced dislocation structure have taken place using TEM due to the ability to directly image the dislocation loops. While this technique allows for the evaluation of the loop size distribution, the low volume of material sampled reduces the statistical significance of any measurement made of number or dislocation line density, in addition to the difficulty in counting dislocation loops when their



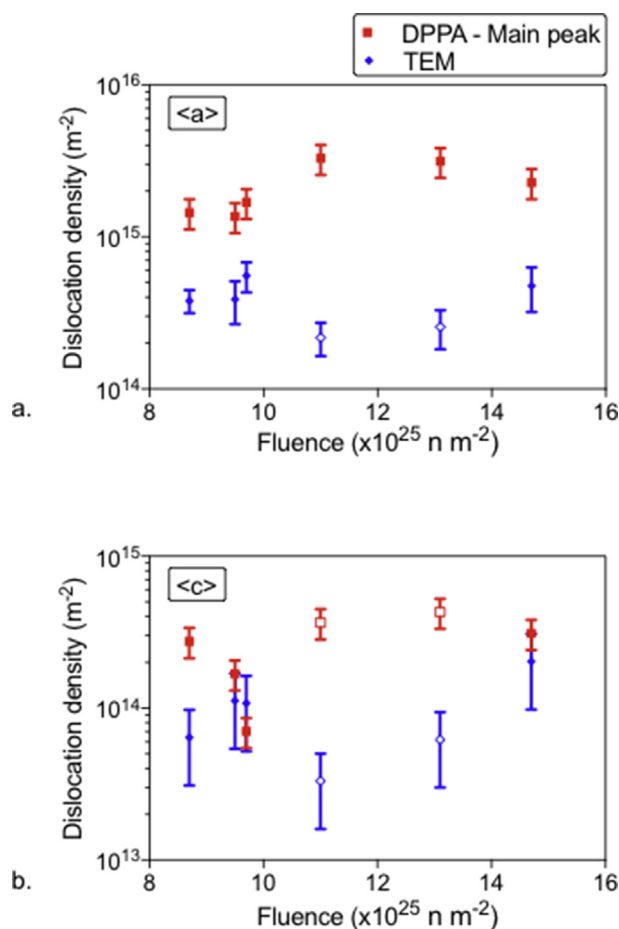


**Fig. 14.** Dislocation densities as a function of fluence as determined by CMWP for the main peak (red) and from TEM measurements (blue) for a. *a* loops and b. *c* loops. The cladding and channel samples are represented by filled and hollow symbols, respectively. (For interpretation of the references to colour in this figure legend, the reader is referred to the web version of this article.)

number density is very high. Diffraction peak profile analysis provides a complementary technique to TEM to determine statistically reliable dislocation densities.

### 5.1. Possible source of peak asymmetry and peak tail shoulders in irradiated material

The diffraction profile is derived from the relative positions of atoms throughout the whole diffracting volume; therefore the peak shapes, positions and intensities, and the background can provide information from all features within this volume across a wide range of length scales. In this study, this has resulted in the unexpected production of secondary peaks and it is important that these peaks are considered in the analysis and that potential sources are discussed.

Inspection of the diffraction profiles in Fig. 6, particularly for some basal peaks, suggests the presence of a second peak in the tails of the Bragg reflections. Such a shoulder has also been observed recently in proton irradiated Zircaloy-2 [25]. As this shoulder is not present in the non-irradiated profiles, it can be concluded that this feature is an irradiation-induced effect. These shoulders could potentially be caused by a number of mechanisms: diffuse scattering from small point defect clusters or dislocation loops [42,57,58]; diffuse scattering from severely distorted regions around small, growing coherent precipitates [59,60]; peak

asymmetry due to stacking faults created by the formation of *c* dislocation loops [28,29]; peak asymmetry due to the arrangement of dislocations into dipoles [61–63]; or from regions with the Zr matrix in a different strain state relative to the bulk.

It might seem surprising that such shoulders are reported for the first time in this work, but this may be explained by the extremely low levels of instrumental broadening and background provided by I11 at Diamond. In addition, these shoulders are likely to be only observable when investigating irradiated material that had been recrystallised. For example if the shoulders were caused by vacancy clusters, cold-worked zirconium alloys (Balogh et al. 2012) have vacancy sinks in the form of *c* dislocations induced from mechanical deformation, which would absorb vacancies preventing formation of clusters. However, the width of these shoulders is thought to be too small to be caused by something the size of sub-microscopic point defect clusters and therefore much larger shoulder features would be expected if this were to be the case [57,58]. Peak asymmetry due to stacking faults is also thought unlikely as these shoulders have been seen in proton irradiated Zircaloy-2 in the absence of faulted *c* dislocation loops [25]. The diffraction order dependence of asymmetry that would be caused by the presence of dislocation dipoles [61–63] is not observed.

The three most plausible causes of the shoulders are that they are due to the presence of strained regions within the material, perhaps associated with dissolved solute elements around precipitates [64,65]; that the precipitation of nanorods or small coherent precipitates [25,66] induces distortion in the surrounding matrix that produces diffuse scattering phenomena similar to that observed in age hardened alloys [59,60]; or that an excess of interstitial *a* loops, which is a possibility at reactor temperatures [11,67], creates regions with an increased lattice parameter. Extensive further investigations will need to be conducted in order to determine the actual source of these features.

Considering the three possible explanations above, it seems reasonable to apply a multiple phase fit when using CMWP, which allows the shoulders to be treated as a second phase, regardless of their origin. The resulting fits are far superior to only using a single peak (i.e. single phase) fit as it can be seen by comparing the varying *M* fit in Fig. 8a and b. Furthermore it can be seen that the shoulders do extend the tails, by comparing the varying *M* fit in Fig. 8a with the main peak fit in Fig. 8b, which increases the calculated dislocation densities. It is also interesting to note that the shoulders sit towards a larger *d*-spacing, which would support the possibility that they arise due to dissolved iron from second phase particle widening the lattice locally.

### 5.2. Dislocation evolution of neutron irradiated Zircaloy-2

As the origin of the shoulders is unknown, the fit to the shoulders is not treated as representing a second phase in this work, but merely as a means to obtaining a more accurate fit to the main Bragg peak. It is possible that the models used in CMWP do not validly describe the secondary peaks and as such the resulting dislocation density values of this 'second phase' are omitted here.

The DPPA analysis suggests that cladding material shows a small increase in dislocation density for *a* loops with increasing fluence during breakaway growth. Previous TEM and irradiation hardening analysis of samples at intermediate fluences preceding breakaway growth has suggested saturation of *a* loop dislocation density [15,68,69]. There are far fewer quantitative experimental investigations into the evolution of the *a* loops during breakaway growth. It is generally assumed that *a* loops remain saturated and that further growth is driven by the *a* shear component of the *c* loops, which increase in number [70]. However, it is difficult to see how the relatively small *a* shear component of *c* loops can indeed

contribute to the significant growth strain during breakaway conditions. The TEM results presented here appear to show an initial increase in  $a$  loop dislocation density before saturating, the differences between the dislocation densities being minor and within error. In contrast the  $c$  loop dislocation density clearly increases, though the total line density remains small. Therefore, TEM results are in agreement with observations made previously in similar studies [15,70]. However the DPPA results presented here contradict this suggestion, by indicating that  $a$  loops continue to grow, either in size or number, during breakaway growth. As the pre-breakaway macroscopic growth strain is produced by the formation of  $a$  loops [71] it seems reasonable that the  $a$  loop dislocation density would continue to increase when the material continues to grow and indeed the linear increase in growth of the clad matches the linear increase in  $a$  loop dislocation density.

The large sources of error in counting  $a$  loops in the TEM, and the possibility of missing  $a$  loops buried under contrast from other sources, is one reason proposed for why there is a discrepancy between the two measurement methods. It should for example be kept in mind that the  $c$  loop dislocation diameter is generally larger than the thickness of the foil resulting in very large uncertainties when undertaking quantitative edge on analysis of  $c$  loops.

The difference in the dislocation density trends of the cladding and channel is difficult to explain and is not explicable when considering the difference in irradiation environment. It has been demonstrated that a lower irradiation temperature (the case for channel material) delays the onset of the formation of  $c$  loops [5–7] and this would reduce the  $c$  loop dislocation density for a given temperature; conversely a lower irradiation temperature increases the number density and decreases the  $a$  loop diameter, therefore increasing the linear dislocation density of  $a$  loops [11,12,72]. From DPPA the  $a$  loop dislocation density of the channel, relative to the clad, is increased, in line with predictions, but the  $c$  loop dislocation density is also increased, contrary to predictions; for the TEM measurements this situation is reversed.

If the  $a$  loops are assumed to have a reasonable value of ellipticity of 1.5 [11,53], i.e. the major axis aligned parallel to [0001] is 50% larger than the minor axis, then the DPPA dislocation density values are changed. The total dislocation densities and  $\{a\}$  loop dislocation densities increase and decrease by approximately 20% and 7% respectively, however, the  $c$  loop density increases by a factor of 2 as a result of the 30% decrease in the  $a$  loop fraction to values in the region of 0.7. Despite these quantitative alterations, the trends remain the same and therefore the above discussion remains valid under the assumption of elliptical loops, with the exception of a greater discrepancy between the  $a$  loop fractions measured by TEM and DPPA.

In Fig. 11 the Wilkens arrangement parameter,  $M$ , is shown to decrease and plateau after  $8.7 \times 10^{25} \text{ n m}^{-2}$  for the cladding sample. The plateau is approximately at a value of 3, similar to the  $M$  value of neutron-irradiated Zr-2.5Nb [21], but greater than typical values for mechanically deformed zirconium and titanium alloys of between 1 and 3 [21,73]. The decrease in  $M$  with increasing neutron fluence suggests that the dislocation loops acquire a stronger dipole character, i.e. the range of the strain field associated with a dislocation loop becomes shorter. The diffraction data recorded on the channel samples display even lower  $M$  values. Mean  $a$  loop diameters were found to be 6 nm for the lowest fluence clad sample, decreasing to 4 nm for the other clad samples, while channel samples had  $a$  loops 3.5 nm in diameter [35–37]. Mean  $c$  loop diameters were 90–120 nm, with no apparent dependence on fluence or sample type. This correlation between  $a$  loop diameter and  $M$  could either be due to the increased screening of the displacement field by opposite sides of the loop as the loop diameter decreases, or that the smaller the loops the more closely

they can be packed thereby reducing  $M$ . Arrangement of  $a$  loops into rows parallel to the basal plane has been observed previously in neutron-irradiated Zircaloy-2 [74], but this was not observed in these samples. No similar correlation is evident between loop density and  $M$ .

### 5.3. Comparison of absolute dislocation density obtained by DPPA and TEM

The calculated dislocation densities determined by DPPA using the multi peak fitting approach showed a large discrepancy in magnitude compared with the dislocation densities as measured by TEM. A number of hypotheses for the difference were explored; however it is expected that there would be some disagreement between the two sets of data for the following reasons. The quantification of dislocation densities via TEM can prove very difficult [17,67] and could provide an underestimate of the true density due to bias in counting and the annihilation of some dislocations to free surfaces in the thinnest regions during electro-polishing. In contrast, the area sampled by X-ray diffraction is much larger than the electron transparent region and thus may be more representative of the bulk material. It is possible that a small amount of strain broadening is contributed from sources other than dislocations [75], which could make the dislocation density estimate by CMWP an overestimate of the true density. However, given the very high dislocation density present in the current case it is likely that these other strain contributions would be negligible [21,76,77].

The above explanations could explain small differences in the values measured by TEM and those determined by CMWP, but not necessarily factors of 4–10 times. Therefore, it is highly unlikely that counting bias, dislocation annealing (TEM) or minor contributions to strain broadening from other sources (CMWP) would cause this disagreement. Moreover, good agreement has been found between previously DPPA and TEM measurements in terms of dislocation density, in mechanically deformed materials [78] and in neutron-irradiated Zr-2.5Nb pressure tube [79].

Various studies have shown that dislocations are often decorated with alloying elements [18,80], primarily fast diffusing iron, which could alter the local strain fields generated by the dislocations, and indeed solute segregation to dislocation loops has been observed in this material [81]. In a phenomenological approach, it could be suggested that the decoration of dislocation loops with alloying elements would introduce additional matrix strain around the dislocation, thereby increasing the stored elastic energy  $\epsilon_L^2$ . While this would increase the energy of the dislocation, it may still be the favourable state due to a concurrent decrease in the total system strain energy by removing the alloying element from the matrix, the decrease in energy in the matrix being larger than the extra strain energy of the dislocation. However any reasonable increase in  $\epsilon_L^2$  reduces the total dislocation density by a negligible amount. In order to bring the absolute dislocation densities determined by CMWP in line with the TEM analysis,  $\epsilon_L^2$  values would need to almost quadruple, which is unreasonable.

It could be suggested that the theory behind DPPA, which was developed for straight dislocations, is unsuitable for application to dislocation loops and that this could lead to a serious misinterpretation of the peak broadening. However, the Krivoglaz-Wilkens model [41–44] is based on strain fields described by the continuum dislocation theory, meaning that an inner cut-off radius is assigned to the line defects corresponding to the size of the dislocation core. A dislocation loop can be interpreted as a curved linear defect when the distance between parallel line segments, i.e. the diameter of the defect, is significantly larger than the dislocation core. The size of the inner cut-off radius is comparable to the length of the Burgers vector, which is  $\sim 0.3 \text{ nm}$  for Zr, meaning that the Krivoglaz-Wilkens

model applies to defect clusters larger than  $\sim 1$  nm, as loops smaller than this practically cannot be considered line defects anymore. The  $a$  loops observed in this material are significantly greater than this [35–37] and therefore CMWP is suitable for evaluation of these diffraction patterns.

The largest disagreement between results obtained by the two methods is that of the dislocation densities of the channel samples, which are clearly greater than the densities for the cladding samples in DPPA, but show lower dislocation density when measured by TEM. However, there is supporting evidence for the DPPA values from Fig. 7, the modified Williamson–Hall plots, which clearly demonstrates that there is a greater slope for the channel sample plot compared to the cladding sample plot. A greater slope indicates more stored energy, which in these samples suggests a larger dislocation density, in-line with the results from DPPA.

The discussion above highlights that there is no obvious explanation for the discrepancy in absolute dislocation densities between DPPA and TEM and more work is needed. Nevertheless, DPPA is measuring real features produced by irradiation, which are not just limited to dislocation loops, but may still be relevant to irradiation growth. While this comparison invites a number of difficult questions, a study of the evolution of these features could provide further insight into the irradiation growth mechanism. One of the issues with the current set of neutron-irradiated samples is that relatively small differences in dislocation densities were expected according to the TEM analysis, due to the fluence levels available. Future work will focus on proton-irradiated samples where a systematic study of the early stage of irradiation damage evolution can be captured and more significant differences are expected with increasing displacements per atom levels.

## 6. Conclusions

The dislocation structure of neutron-irradiated Zircaloy-2 has been investigated by diffraction peak profile analysis of synchrotron X-ray diffraction patterns and compared to transmission electron microscopy measurements. Despite the challenges pointed out here, the diffraction peak profile analysis provides highly valuable information regarding the analysis of defect structures in irradiated zirconium alloys, which in some cases challenges the TEM observations or provides complimentary information that cannot be obtained by TEM. The main findings of this work can be summarised as follows:

- An unknown feature is present in the diffraction patterns as shoulders or induced peak asymmetry, which are believed to form either due to strained regions within the matrix formed by dissolving precipitates, an excess of interstitial loops increasing the lattice parameter locally, or due to diffuse scattering from severely distorted regions surrounding nucleating precipitates.
- For the cladding and channel material analysed here, the dislocation densities are not comparable when plotted as a function of neutron fluence.
- There is a discrepancy of up to an order of magnitude in the dislocation density of  $a$  loops as determined by DPPA compared to TEM measurements, whereas for the cladding samples the dislocation density of  $c$  loops are more comparable. Possible explanations for these differences have been discussed.
- DPPA suggest that the claddings' total dislocation density increases with fluence correlating with the linear breakaway growth strain. This trend is not seen in the case of the TEM analysis.
- The  $a$  loop dislocation densities calculated by diffraction peak profile analysis also increase with fluence, in opposition to dislocation density evolution recorded by TEM measurements,

which appear to show a saturation of  $a$  loop dislocation density. The  $c$  loop dislocation density evolution is more complex and shows no clear trend from DPPA but appears to show a long-term increase as determined by TEM.

## Acknowledgements

The majority of this work has been funded by an EPSRC Leadership Fellowship (EP/I005420/1) with industrial financial and material contributions from Westinghouse Electric and Studsvik Nuclear AB. G.R is grateful for the partial support of the French State through the program "Investment in the future" operated by the National Research Agency (ANR) and referenced as ANR-11-LABX-0008-01, LabEx-DAMAS. The authors would like to thank Diamond Light Source for beam time at beamline I11 (EE8395 and EE10006). The authors would also like to thank Allan Harte, Matthew Topping, Elisabeth Francis and Christopher Race for their assistance at experiments and for useful discussions. All data presented in this paper can be obtained on request.

## References

- [1] M. Griffiths, Microstructure evolution in Zr alloys during irradiation: dose, dose rate, and impurity dependence, *J. ASTM Int.* 5 (2008) 19–26.
- [2] R.A. Holt, In-reactor deformation of zirconium alloy components, *J. ASTM Int.* 5 (2008) 3–18.
- [3] M.A. McGrath, S. Yagnik, Experimental investigation of irradiation creep and growth of recrystallized Zircaloy-4 guide tubes pre-irradiated in PWR, *J. ASTM Int.* 5 (2011) 875–898.
- [4] R.A. Holt, R.W. Gilbert,  $c$  component dislocations in annealed Zircaloy irradiated at about 570 K, *J. Nucl. Mater.* 137 (1986) 185–189.
- [5] M. Griffiths, R.W. Gilbert, V. Fidleris, R.P. Tucker, R.B. Adamson, Neutron damage in zirconium alloys irradiated at 644 to 710 K, *J. Nucl. Mater.* 150 (1987) 159–168.
- [6] M. Griffiths, R.W. Gilbert, V. Fidleris, Accelerated irradiation growth of zirconium alloys, in: L.F.P. Van Swam, C.M. Eucken (Eds.), *Zircon. Nucl. Ind. Eighth Int. Symp.*, ASTM, Philadelphia, PA, 1989, pp. 658–677.
- [7] R.P. Tucker, V. Fidleris, R.B. Adamson, High-fluence irradiation growth of zirconium alloys at 644 to 725 K, in: D.G. Franklin, R.B. Adamson (Eds.), *Zircon. Nucl. Ind. Sixth Int. Symp.*, ASTM, Philadelphia, PA, 1984, pp. 427–451.
- [8] R.B. Adamson, R.P. Tucker, V. Fidleris, High-temperature irradiation growth in Zircaloy, in: D.G. Franklin (Ed.), *Zircon. Nucl. Ind. Fifth Conf.*, ASTM, Philadelphia, PA, 1982, pp. 208–234.
- [9] A. Rogerson, Irradiation growth in zirconium and its alloys, *J. Nucl. Mater.* 159 (1988) 43–61.
- [10] P.M. Kelly, R.G. Blake, The characterization of dislocation loops in neutron irradiated zirconium, *Philos. Mag.* 28 (1973) 415–426.
- [11] A. Jostons, P.M. Kelly, R.G. Blake, The nature of dislocation loops in neutron irradiated zirconium, *J. Nucl. Mater.* 66 (1977) 236–256.
- [12] D.O. Northwood, R.W. Gilbert, L.E. Bahen, P.M. Kelly, R.G. Blake, A. Jostons, et al., Characterization of neutron irradiation damage in zirconium alloys – an international "round-robin" experiment, *J. Nucl. Mater.* 79 (1979) 379–394.
- [13] R.A. Murgatroyd, A. Rogerson, Irradiation growth in cold-worked Zircaloy-2, in: T.P. Papazoglou (Ed.), *Zircon. Nucl. Ind. Fourth Int. Symp.*, ASTM, Philadelphia, PA, 1979, pp. 213–226.
- [14] J. Williams, E.C. Darby, D.C.C. Minty, Irradiation growth of annealed Zircaloy-2, in: D.G. Franklin, R.B. Adamson (Eds.), *Zircon. Nucl. Ind. Sixth Int. Symp.*, ASTM, Philadelphia, PA, 1984, pp. 376–393.
- [15] G.J.C. Carpenter, D.O. Northwood, The contribution of dislocation loops to radiation growth and creep of Zircaloy-2, *J. Nucl. Mater.* 56 (1975) 260–266.
- [16] A. Rogerson, R.A. Murgatroyd, "Breakaway" growth in annealed Zircaloy-2 at 353 K and 553 K, *J. Nucl. Mater.* 113 (1983) 256–259.
- [17] M. Griffiths, R.W. Gilbert, The formation of  $c$ -component defects in zirconium alloys during neutron irradiation, *J. Nucl. Mater.* 150 (1987) 169–181.
- [18] Y. de Carlan, C. Regnard, M. Griffiths, D. Gilbon, C. Lemaignan, Influence of iron in the nucleation of ( $c$ ) component dislocation loops in irradiated Zircaloy-4, in: E.R. Bradley, G.P. Sabol (Eds.), *Zircon. Nucl. Ind. Elev. Int. Symp.*, ASTM, West Conshohocken, PA, 1996, pp. 638–653.
- [19] G. Ribárik, J. Gubicza, T. Ungár, Correlation between strength and microstructure of ball-milled Al–Mg alloys determined by X-ray diffraction, *Mater. Sci. Eng. A* 387–389 (2004) 343–347.
- [20] T. Ungár, O. Castelnau, G. Ribárik, M. Drakopoulos, J.L. Béchéde, T. Chauveau, et al., Grain to grain slip activity in plastically deformed Zr determined by X-ray micro-diffraction line profile analysis, *Acta Mater.* 55 (2007) 1117–1127.
- [21] L. Balogh, D.W. Brown, P. Mosbrucker, F. Long, M.R. Daymond, Dislocation structure evolution induced by irradiation and plastic deformation in the Zr–2.5Nb nuclear structural material determined by neutron diffraction line profile analysis, *Acta Mater.* 60 (2012) 5567–5577.



- [22] I.C. Dragomir, G.A. Castello-Branco, G. Ribárik, H. Garmestani, T. Ungár, R.L. Snyder, Burgers vector populations in hot rolled titanium determined by X-ray peak profile analysis, *Z. Für Krist.* (2006) 99–104.
- [23] T. Ungár, S. Ott, P.G. Sanders, A. Borbély, J.R. Weertman, Dislocations, grain size and planar faults in nanostructured copper determined by high resolution X-ray diffraction and a new procedure of peak profile analysis, *Acta Mater.* 46 (1998) 3693–3699.
- [24] S. Valizadeh, G. Ledergerber, S. Abolhassan, D. Jädnäs, M. Dahlbäck, E.V. Mader, et al., Effects of secondary phase particle dissolution on the in-reactor performance of BWR cladding, *J. ASTM Int.* 8 (2011) 103025.
- [25] A. Harte, T. Seymour, E.M. Francis, P. Frankel, S.P. Thompson, D. Jädnäs, et al., Advances in synchrotron x-ray diffraction and transmission electron microscopy techniques for the investigation of microstructure evolution in proton- and neutron-irradiated zirconium alloys, *J. Mater. Res.* 30 (2015) 1349–1365.
- [26] S.P. Thompson, J.E. Parker, J. Potter, T.P. Hill, A. Birt, T.M. Cobb, et al., Beamline I11 at Diamond: a new instrument for high resolution powder diffraction, *Rev. Sci. Instrum.* 80 (2009).
- [27] G. Ribárik, T. Ungár, J. Gubicza, MWP-fit: a program for multiple whole-profile fitting of diffraction peak profiles by ab initio theoretical functions, *J. Appl. Crystallogr.* 34 (2001) 669–676.
- [28] L. Balogh, G. Ribárik, T. Ungár, Stacking faults and twin boundaries in fcc crystals determined by x-ray diffraction profile analysis, *J. Appl. Phys.* 100 (2006) 23512.
- [29] L. Balogh, G. Tichy, T. Ungár, Twinning on pyramidal planes in hexagonal close packed crystals determined along with other defects by X-ray line profile analysis, *J. Appl. Crystallogr.* 42 (2009) 580–591.
- [30] F. Nagase, T. Chuto, T. Fuketa, Ring compression ductility of high-burnup fuel cladding after exposure to simulated LOCA conditions, *J. Nucl. Sci. Technol.* 48 (2011) 1369–1376.
- [31] D.R. Olander, Light water reactor fuel design and performance, in: K.H.J. Buschow (Ed.), *Encycl. Mater. Sci. Technol.*, Elsevier, Amsterdam; New York, 2001, pp. 4490–4502.
- [32] V. Fidleris, R.P. Tucker, R.B. Adamson, An overview of microstructural and experimental factors that affect the irradiation growth behavior of zirconium alloys, in: R.B. Adamson, L.F.P. Van Swam (Eds.), *Zircon. Nucl. Ind. Seventh Int. Symp.*, ASTM, Philadelphia, PA, 1987, pp. 49–85.
- [33] M. Blat-Yrieix, A. Ambard, F. Foc, A. Miquet, S. Beguin, N. Cayet, Toward a better understanding of dimensional changes in Zircaloy-4: what is the impact induced by hydrides and oxide layer? *J. ASTM Int.* 5 (2008) 594–611.
- [34] C.C. Tang, S.P. Thompson, T.P. Hill, G.R. Wilken, U.H. Wagner, Design of powder diffraction beamline (BL-111) at Diamond, *Z. Für Krist. Suppl.* 26 (2007) 153–158.
- [35] D. Jädnäs, SPP and Dislocation Analysis Using TEM of Westinghouse Zry-2 Fuel Channel Samples Irradiated in OL2, Report STUDEVIK/N-10/121, Studsvik Nuclear AB, 2009.
- [36] D. Jädnäs, SPP and Dislocation Analysis Using TEM of Westinghouse Zry-2 Fuel Channel Samples Irradiated in KKL and OL2, Report STUDEVIK/N-10/060, Studsvik Nuclear AB, 2009.
- [37] D. Jädnäs, SPP and Dislocation Analysis Using TEM of Westinghouse Zry-2 LK3 Fuel Cladding Samples Irradiated in KKL, Report STUDEVIK/N-09/218, Studsvik Nuclear AB, 2009.
- [38] K. Jakoubovskii, K. Mitsuishi, Y. Nakayama, K. Furuya, Mean free path of inelastic electron scattering in elemental solids and oxides using transmission electron microscopy: atomic number dependent oscillatory behavior, *Phys. Rev. B - Condens. Matter Mater. Phys.* 77 (2008) 1–7.
- [39] T. Ungár, A. Borbély, The effect of dislocation contrast on X-ray line broadening: a new approach to line profile analysis, *Appl. Phys. Lett.* 69 (1996) 3173.
- [40] T. Ungár, The meaning of size obtained from broadened X-ray diffraction peaks, *Adv. Eng. Mater.* 5 (2003) 323–329.
- [41] M.A. Krivogla, Theory of X-ray and Thermal Neutron Scattering by Real Crystals, Plenum Press, New York, 1969.
- [42] M.A. Krivogla, X-ray and Neutron Diffraction in Nonideal Crystals, Springer-Verlag, Berlin, 1996.
- [43] M. Wilkens, Fundamental Aspects of Dislocation Theory, vol. II, Spec. Publ. Natl. Bur. Stand. (US), Washington DC, 1970.
- [44] M. Wilkens, The determination of density and distribution of dislocations in deformed single crystals from broadened X-ray diffraction profiles, *Phys. Stat. Sol.* 2 (1970) 359–370.
- [45] T. Ungár, I. Dragomir, Á. Révész, A. Borbély, The contrast factors of dislocations in cubic crystals: the dislocation model of strain anisotropy in practice, *J. Appl. Crystallogr.* 32 (1999) 992–1002.
- [46] T. Ungár, G. Tichy, The effect of dislocation contrast on X-ray line profiles in untextured polycrystals, *Phys. Status Solidi* 171 (1999) 425–434.
- [47] P. Klimanek, R. Kužel Jr., X-ray diffraction line broadening due to dislocations in non-cubic materials. I. General considerations and the case of elastic isotropy applied to hexagonal crystals, *J. Appl. Crystallogr.* 21 (1988) 59–67.
- [48] M. Wilkens, X-ray line broadening and mean square strains of straight dislocations in elastically anisotropic crystals of cubic symmetry, *Phys. Status Solidi* 104 (1987) 1–6.
- [49] I.C. Dragomir, T. Ungár, Contrast factors of dislocations in the hexagonal crystal system, *J. Appl. Crystallogr.* 35 (2002) 556–564.
- [50] I.C. Dragomir, A. Borbély, T. Ungár, Contrast factors and character of dislocations in cubic and hexagonal crystals, *Mater. Sci. Forum* 443–444 (2004) 95–98.
- [51] A. Borbély, J. Dragomir-Cernatescu, G. Ribárik, T. Ungár, Computer program ANIZC for the calculation of diffraction contrast factors of dislocations in elastically anisotropic cubic, hexagonal and trigonal crystals, *J. Appl. Crystallogr.* 36 (2003) 160–162.
- [52] K. Máthi, K. Nyilas, A. Axt, I. Dragomir-Cernatescu, T. Ungár, P. Lukács, The evolution of non-basal dislocations as a function of deformation temperature in pure magnesium determined by X-ray diffraction, *Acta Mater.* 52 (2004) 2889–2894.
- [53] L. Balogh, F. Long, M.R. Daymond, Contrast factors of irradiation induced dislocation loops in hexagonal materials, *J. Appl. Crystallogr.* 49 (2016) 2184–2200.
- [54] E.H. Yoffe, The angular dislocation, *Philos. Mag.* 5 (1960) 161–175.
- [55] X.Y. Meng, D.O. Northwood, Second phase particles in Zircaloy-2, *J. Nucl. Mater.* 168 (1989) 125–136.
- [56] G.K. Williamson, W.H. Hall, X-ray line broadening from filed aluminium and wolfram, *Acta Metall.* 1 (1953) 22–31.
- [57] P. Ehrhart, Investigation of radiation damage by X-ray diffraction, *J. Nucl. Mater.* 216 (1994) 170–198.
- [58] B.C. Larson, X-ray diffuse scattering near Bragg reflections for the study of clustered defects in crystalline materials, in: *Diffus. Scatt. Fundam. Prop. Mater.*, 2009, pp. 139–160.
- [59] C.R. Houska, X-ray scattering from systems in early stages of precipitation, *Acta Crystallogr. Sect. A Found. Crystallogr.* 49 (1993) 771–781.
- [60] R. Kužel, B. He, C.R. Houska, Characterization of severe matrix distortions during phase separation from the redistribution of diffracted intensities, *J. Mater. Sci.* 32 (1997) 2451–2467.
- [61] H. Mughrabi, T. Ungár, W. Kienle, M. Wilkens, Long-range internal stresses and asymmetric X-ray line-broadening in tensile-deformed [001]-orientated copper single crystals, *Philos. Mag. A* 53 (1986) 793–813.
- [62] T. Ungár, I. Groma, M. Wilkens, Asymmetric X-ray line broadening of plastically deformed crystals. II. Evaluation procedure and application to [001]-Cu crystals, *J. Appl. Crystallogr.* 22 (1989) 26–34.
- [63] I. Groma, G. Monnet, Analysis of asymmetric broadening of X-ray diffraction peak profiles caused by randomly distributed polarized dislocation dipoles and dislocation walls, *J. Appl. Crystallogr.* 35 (2002) 589–593.
- [64] F. Garzarolli, W. Goll, A. Seibold, I. Ray, Effect of in-PWR irradiation on size, structure, and composition of intermetallic precipitates of Zr alloys, in: E.R. Bradley, G.P. Sabol (Eds.), *Zircon. Nucl. Ind. Elev. Int. Symp.*, ASTM, West Conshohocken, PA, 1996, pp. 541–556.
- [65] G.P. Kobylansky, A.E. Novoselov, A.V. Obukhov, Z.E. Ostrovsky, V.N. Shishov, M.M. Peregud, et al., Radiation damage of E635 alloy under high dose irradiation in the VVER-1000 and BOR-60 reactors, *J. ASTM Int.* 8 (2011) 827–850.
- [66] A. Harte, A Comparison of Proton and Neutron Irradiation-induced Microstructural and Microchemical Evolution in Zircaloy-2, PhD, The University of Manchester, 2015.
- [67] M. Griffiths, A review of microstructure evolution in zirconium alloys during irradiation, *J. Nucl. Mater.* 159 (1988) 190–218.
- [68] B.V. Cockeram, R.W. Smith, K.J. Leonard, T.S. Byun, L.L. Snead, Development of microstructure and irradiation hardening of Zircaloy during low dose neutron irradiation at nominally 358°C, *J. Nucl. Mater.* 418 (2014) 46–61.
- [69] B.V. Cockeram, K.J. Leonard, T.S. Byun, L.L. Snead, J.L. Hollenbeck, Development of microstructure and irradiation hardening of Zircaloy during low dose neutron irradiation at nominally 377–440°C, *J. Nucl. Mater.* 449 (2014) 69–87.
- [70] M. Griffiths, J.F. Mecke, J.E. Winegar, Evolution of microstructure in zirconium alloys during irradiation, in: E.R. Bradley, G.P. Sabol (Eds.), *Zircon. Nucl. Ind. Elev. Int. Symp.*, ASTM, West Conshohocken, PA, 1996, pp. 580–602.
- [71] C.H. Woo, Modeling irradiation growth of zirconium and its alloys, *Radiat. Eff. Defects Solids Inc. Plasma Sci. Plasma Technol.* 144 (1998) 145–169.
- [72] R.W. Gilbert, K. Farrell, C.E. Coleman, Damage structure in zirconium alloys neutron irradiated at 573 to 923 K, *J. Nucl. Mater.* 84 (1979) 137–148.
- [73] I.C. Dragomir, D.S. Li, G.A. Castello-Branco, H. Garmestani, R.L. Snyder, G. Ribárik, et al., Evolution of dislocation density and character in hot rolled titanium determined by X-ray diffraction, *Mater. Charact.* 55 (2005) 66–74.
- [74] D.O. Northwood, R.W. Gilbert, Some comments on damage alignment in neutron-irradiated zirconium alloys, *J. Nucl. Mater.* 51 (1974) 271–276.
- [75] T. Ungár, G. Tichy, J. Gubicza, R.J. Hellmig, Correlation between subgrains and coherently scattering domains, *Powder Diffr.* 20 (2005) 366–375.
- [76] T. Ungár, Dislocation densities, arrangements and character from X-ray diffraction experiments, *Mater. Sci. Eng. A* 309–310 (2001) 14–22.
- [77] T. Ungár, Microstructural parameters from X-ray diffraction peak broadening, *Scr. Mater.* 51 (2004) 777–781.
- [78] T. Ungár, E. Schafner, P. Hanak, S. Bernstorff, M. Zehetbauer, Vacancy production during plastic deformation in copper determined by in situ X-ray diffraction, *Mater. Sci. Eng. A* 462 (2007) 398–401.
- [79] Y.S. Kim, S.S. Kim, Y.M. Cheong, K.S. Im, Determination of dislocation density and composition of  $\beta$ -Zr in Zr-2.5Nb pressure tubes using X-ray and TEM, *J. Nucl. Mater.* 317 (2003) 117–129.
- [80] M. Griffiths, R.A. Holt, A. Rogerson, Microstructural aspects of accelerated deformation of Zircaloy nuclear reactor components during service, *J. Nucl. Mater.* 225 (1995) 245–258.
- [81] A. Harte, D. Jädnäs, M. Topping, P. Frankel, C. Race, J. Romero, L. Hallstadius, E.C. Darby, M. Preuss, The effect of matrix chemistry on dislocation evolution in an irradiated Zr alloy, *Acta Mater.* (December 2016). Submitted for publication.